Reducing AC Joule Losses in Hairpin Windings of Electric Machines: Strategies for Minimizing Losses Due to Radial and Tangential Flux

1st Yitbarek Bekele
Institute for Drive Systems and Power Electronics
Leibniz University Hannover
Hannover, Germany
Yitbarek.bekele@ial.uni-hannover.de

2nd Olga Korolova
ProFluxx GmbH
Ingolstadt, Germany
Olga.korolova@profluxx.com

3rd Andreas Biebighäuser
ProFluxx GmbH
Ingolstadt, Germany
Andreas.Biebighaeuser@profluxx.com

4th Siddique Akbar
ProFluxx GmbH
Ingolstadt, Germany
orcid.org/0000-0001-7769-6956

5th Amir Ebrahimi
Institute for Electrical Drives, Power Electronics and Devices
University of Bremen
Bremen, Germany
orcid.org/0000-0001-7549-172X

6th Bernd Ponick
Institute for Drive Systems and Power Electronics
Leibniz University Hannover
Hannover, Germany
orcid.org/0000-0002-7762-2209

***Abstract*—This paper presents a comprehensive analysis of conductor design strategies to reduce joule losses in hairpin windings of high-speed permanent magnet synchronous machines (PMSMs). With the increasing demand for high torque density, efficiency, and high-speed operation in electric vehicles and aircraft, minimizing these losses is crucial. Starting with a reference winding layout, various loss mechanisms due to radial and tangential flux components are investigated using finite element analysis (FEA) under both no-load and short-circuit conditions. Design variants including adjustments to conductor geometry, slot opening shapes, layer-specific conductor height tuning and segmented conductor designs with overhang twisting are explored. The findings are relevant for improving the performance and manufacturability of electric machines, with additive manufacturing offering new design opportunities for enhanced efficiency and lower losses.**

***Index Terms*—Eddy Currents, Hairpin Windings, Additive Manufacturing.**

I. Introduction

In recent years, electric machines have experienced increasing adoption as traction drives in the automotive industry. This transformation requires a high degree of automation in production to meet the rising demand. Additionally, in the field of electromobility, electric machines must deliver high torque density due to limited installation space, while also meeting growing demands for high efficiency. To address these challenges, profiled conductors, commonly referred to as hairpins, are now widely used for stator windings in electric machines [1]. Compared to conventional round wires, hairpins offer a higher fill factor, as their rectangular shape conforms better to the stator slots, resulting in a higher ratio of conductor to insulation material or empty space [2], [3]. They also improve heat transfer from the winding to the core and enhance manufacturability, particularly in automated production processes [4], [5].

However, due to the large cross-sectional area of the rectangular conductors, the current density is not evenly distributed, especially when the motor is operating at high speeds [6], [7]. To reduce the skin effect (current displacement) during high frequency operation, parallel paths of subconductors are generally recommended, requiring appropriate design analysis and suitable connection rules [8].

Additive manufacturing (AM), often called 3D printing, is considered one of the key technologies of the 21st century across various industries [9], [10]. Thanks to the layer-by-layer production of additively manufactured components and the associated freedom in design in all three spatial directions, components can take on almost any conceivable geometry. This enables the direct implementation of complex geometries, such as lattice structures or bionic shapes, or functional enhancements, such as special structural properties or heat transfer paths, into the component during production, without the need for forming tools [11].

In the field of electric machine, which has a history spanning almost two centuries, technological advancements in additive processing of metallic materials allow for a reassessment of long-standing design principles. Existing design guidelines and production limitations, which apply to conventional manufacturing technologies, can now be expanded. This paper begins with a brief introduction to the reference machine before exploring strategies to reduce losses in conductors.

Funded by the European Union

This work was supported by the European Union under Marie Sklodowska Curie Doctoral-Industrial Project (HORIZON-MSCA-2021-DN-01) with the title "New Generation of Electrical Machines Enabled by Additive Manufacturing—EMByAM"

II. Reference Machine Specification

To establish a benchmark for comparing research results, a reference machine is defined: a 48-slot, 8-pole permanent magnet synchronous motor (PMSM) with an 8-layer hairpin winding topology. The motor operates at a rated voltage of 450 V and a maximum speed of 15000 min^{-1}. A cross-sectional view of the machine is shown in Fig. 2.

TABLE I
Reference Machine Specification

Machine Type	Permanent Magnet Excited Synchronous Motor
Number of Slots	48
Number of Poles	8
Number of Layers	8
Number of Phases	3
Maximum Operating Speed	15000 min^{-1}
Maximum Frequency	1000 Hz
Rated Voltage	450 V
Rated Power	180 kW
Winding Material	Copper

To facilitate understanding of the conductor arrangement, especially for the methods discussed in later chapters, Fig. 1 illustrates the winding layout for Phase A. The naming convention for the conductors is structured so that the first digit represents the parallel branch number, while the second digit indicates the sequence of the conductor within that branch.

TABLE II
Coil Pitch Patterns for Parallel Branches

	Pitches			
First Branch	7	6	5	6
Second Branch	5	6	7	6
Third Branch	5	6	7	6
Fourth Branch	7	6	5	6

As shown in Fig. 1, the first conductor in the first parallel branch is placed at the bottom layer of slot 1 (denoted 1_1). Its corresponding return conductor, forming the other side of the hairpin, is placed in the second layer of slot 8 (denoted 1_2), resulting in a pitch of 7.

At the ends of each hairpin, the two legs are joined by a weld. The next hairpin begins in slot 14, placed in the first layer, and connects to slot 19, forming a coil pitch of 5. This sequence continues with alternating coil pitches in the order 7, 6, 5 and 6, until one complete round of the stator is covered. Table II summarizes the coil pitch patterns for each parallel branch.

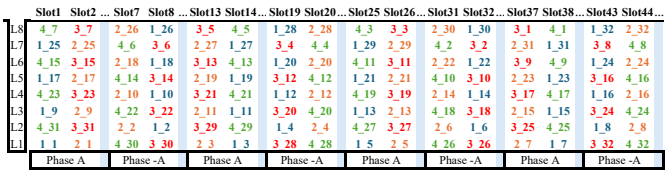

Fig. 1. Hairpin winding layout of reference machine.

After completing one round of the stator, the winding progresses to the third layer, continuing the same pattern but alternating between the third and fourth layers until another full machine turn is completed.

The second parallel branch follows a pattern similar to the first, except it begins at slot 2, and its initial sequence of coil pitches is 5, 6, 7, and 6. For the remaining two parallel branches, two key differences apply: first, their winding direction is reversed compared to the first two branches; second, they alternate from the top layer to the bottom layer rather than from bottom to top.

These design choices ensure that the average radial position of all conductors across the four parallel branches is identical, thereby preventing circulating currents caused by positional imbalances within the slots.

III. Conductor Joule Loss Due to Radial Flux

To understand which measures help minimize power losses due to radial and tangential flux, two separate calculations were performed using FEA in JMAG Designer: no-load and short-circuit, respectively. This section focuses on the no-load case. The reference bare conductor has 1.73 mm x 4 mm cross-section with 0.5 mm fillet radius. Fig. 2(a) shows the no-load calculation, revealing a radial flux that penetrates the conductors in layers 7 and 8 at the slot opening. This results in an increase in eddy current losses at these layers.

Considering the strongly nonlinear behavior of the skin effect at higher frequencies [12] and the potential for increased power density, losses at twice the reference speed were investigated, while mechanical challenges were neglected. Saturation and higher harmonic effects were also not considered. Fig. 3 shows the joule loss density distribution across the eight layers in a slot at 2000 Hz. The winding with the reference conductor

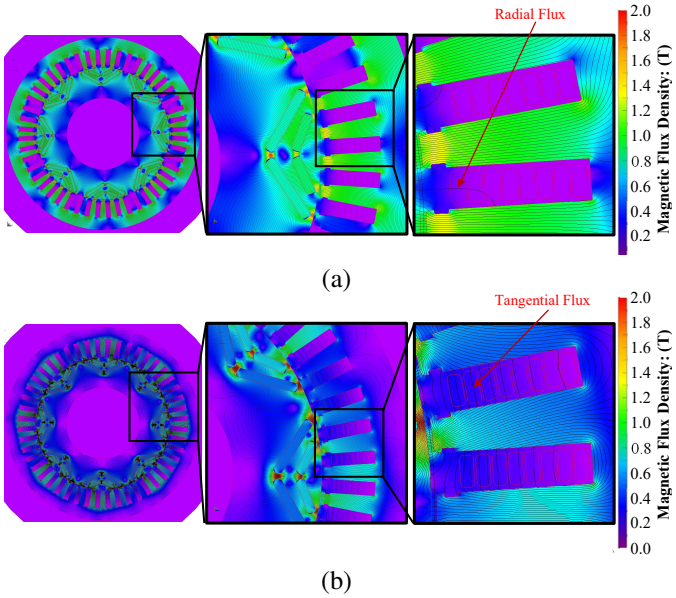

Fig. 2. Magnetic Flux Density Contour Plot (a) No Load (b) Short Circuit.

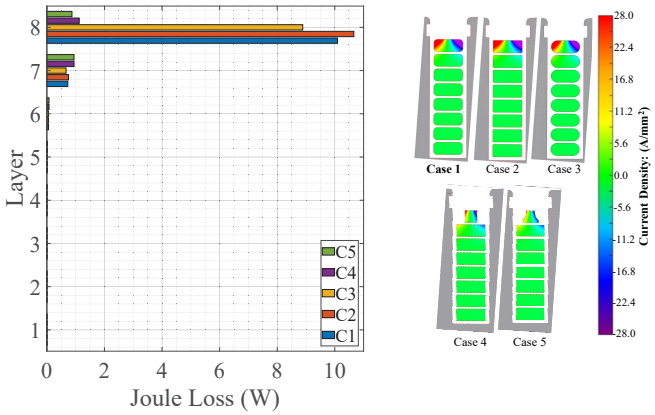

(a) (b)

Fig. 3. No-load calculation with various conductor geometries: (a) loss density plot; (b) current density plot.

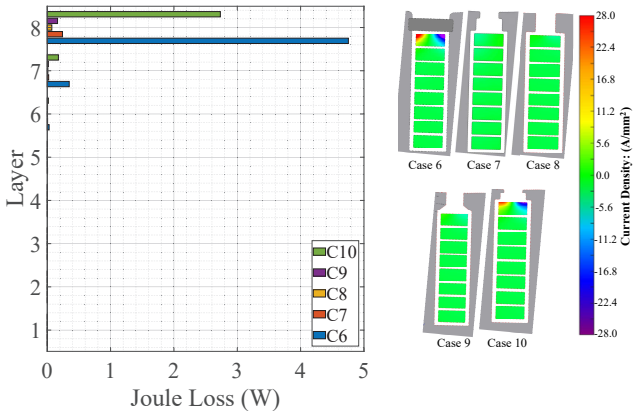

(a) (b)

Fig. 4. No-load calculation with various slot opening geometries: (a) loss density plot; (b) current density plot.

shape (Case 1) exhibits a total loss of 174.3 W per phase, 92.7% of which is from the conductors in layer 8 alone.

Then, with the intention of increasing the copper fill factor, the fillet radius was reduced to 0.1 mm, as such sharp corners can be theoretically achieved using AM techniques. This results in a 3% increase in cross-sectional area. This is Case 2, and unfortunately, at 2000 Hz, the AC loss has increased by 5.4%. This prompts an investigation into the effect of increasing the fillet radius to its maximum value, half of the conductor's height (0.865 mm), as in Case 3. In doing so, 6.4% of copper is removed, but the loss at 2000 Hz has decreased by 11.7% compared to Case 1. Since only the top conductor is mainly affected by the radial flux and thus experiences higher loss, varying the geometry of the top conductor alone is sufficient. Cases 4 and 5 demonstrate this. Although reducing the conductor width helps reduce the loss, as shown in Case 4, shaping it as in Case 5 has a greater effect. Both Case 4 and Case 5 have the same conductor area in layer 8, but the loss in Case 5 is reduced by 91.4%, compared to 88.9% in Case 4.

One advantage of hairpin windings is that they can be inserted into the stator slot in the axial direction, enabling the use of a semi-closed stator slot opening. Various slot opening geometries have been analyzed and are summarized in Fig 4. Case 6 represents the reference slot geometry with the addition of a magnetic wedge (with $\mu_r = 4$), which reduces the copper loss by 55.2% compared to Case 2. Cases 7, 8 and 9 introduce different slot opening variants, resulting in loss reductions of 97.6%, 99.1% and 98.3%, respectively.

In Case 10, the slot opening height of Case 7 is reduced by half, shifting the entire set of conductors closer to the airgap. As a result, the conductor in layer 8 experiences increased radial flux penetration, even though a semi-closed opening is still used. For the upcoming calculations, Case 9 will be used as it is a common slot opening used nowadays [13], [14], [15].

Table III summarizes the loss distributions (in watts) across the slot layers due to radial flux for the discussed cases.

IV. Conductor Joule Loss Due to Tangential Flux

A similar approach was taken to investigate the loss due to tangential flux induced eddy currents. For that, short-circuit calculation was performed. Fig. 2(b) shows the short-circuit calculation, revealing a tangential flux that penetrates the conductors. This section explores different approaches to minimize losses due to tangential flux.

A. Conductor Geometry Variations

It is evident from Fig. 5(a) that the loss increases significantly from layer 1 to layer 8, approaching the slot opening.

TABLE III
Summary of Joule Loss Distribution Across Slot Layers Under Radial Flux Influence

	Case 1		Case 2	Case 3	Case 4	Case 5	Case 6	Case 7	Case 8	Case 9	Case 10
	1000 Hz	2000 Hz	2000 Hz	2000 Hz	2000 Hz	2000 Hz	2000 Hz	2000 Hz	2000 Hz	2000 Hz	2000 Hz
L8	2.90	10.09	10.66	8.89	1.12	0.87	4.75	0.24	0.07	0.16	2.73
L7	0.24	0.73	0.75	0.67	0.94	0.94	0.35	0.02	0.01	0.02	0.18
L6	0.02	0.06	0.06	0.05	0.07	0.07	0.03	0.01	0.00	0.01	0.02
L5	0.00	0.01	0.01	0.01	0.01	0.01	0.01	0.00	0.00	0.00	0.00
L4	0.00	0.00	0.00	0.00	0.00	0.00	0.00	0.00	0.00	0.00	0.00
L3	0.00	0.00	0.00	0.00	0.00	0.00	0.00	0.00	0.00	0.00	0.00
L2	0.00	0.00	0.00	0.00	0.00	0.00	0.00	0.00	0.00	0.00	0.00
L1	0.00	0.00	0.00	0.00	0.00	0.00	0.00	0.00	0.00	0.00	0.00
Total Loss Per Slot (Watt)	3.17	10.89	11.48	9.62	2.16	1.91	5.14	0.28	0.10	0.20	2.94
Total Loss Per Phase (Watt)	50.69	174.30	183.76	153.96	34.56	30.51	82.32	4.51	1.61	3.18	47.04

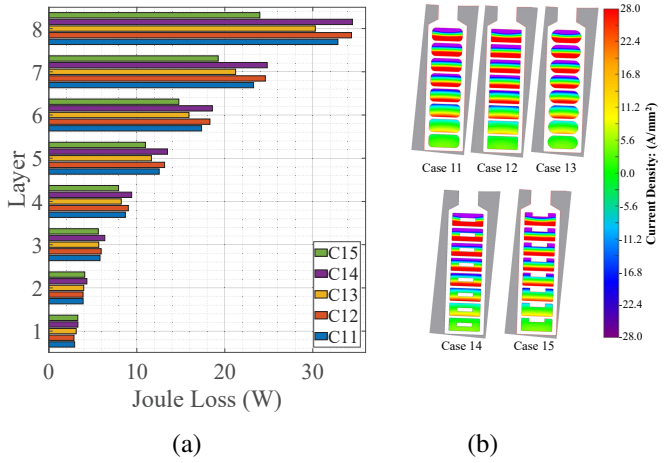

Fig. 5. Short-circuit calculation with various conductor geometries: (a) loss density plot; (b) current density plot.

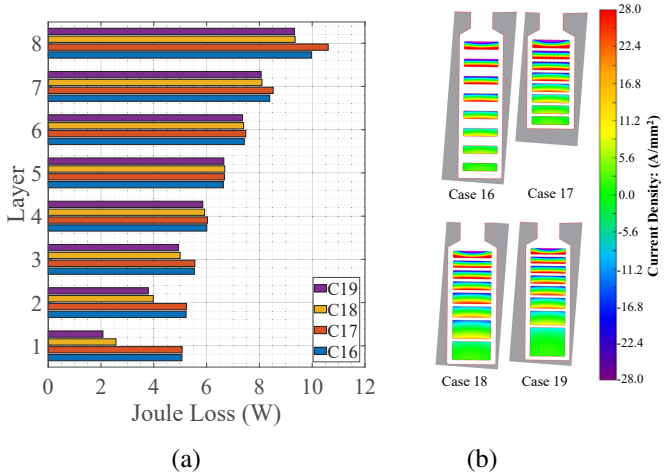

Fig. 6. Short-circuit calculation with various conductor heights: (a) loss density plot; (b) current density plot.

This increase occurs because the AC loss in each conductor is strongly influenced by the ampere-turns located beneath it [6].

For the conductor in layer 1, which has no conductors below it, the loss is primarily due to the magnetic field generated by its own current. This is referred to as a single-sided skin effect [16]. Since the conductor height is below the skin depth, this effect is small, and the losses are primarily due to DC resistance. However, for conductors in layers 2 and above, the losses are higher because these conductors are influenced not only by their own magnetic fields but also by the fields generated by the underlying conductors, a phenomenon known as the double-sided skin effect, which significantly increases AC losses. For example, in Case 11, the AC loss in the conductor at layer 8 is 11.2 times higher than its DC loss.

Similar to the no-load results, the sharp-edged conductor variant (Case 12) shows a 4.5% increase in loss compared to the reference, while the rounded conductor geometry (Case 13) shows a 6.8% decrease. This indicates that increasing the fillet radius of the conductor cross-section helps mitigate eddy currents circulating at the corners, particularly in regions subjected to strong tangential magnetic fields. As demonstrated in Fig. 5(a), conductor geometry has a clear influence on the distribution of losses.

Cases 14 and 15 further investigate the incorporation of internal cooling ducts. The results show that not only the presence but also the placement of the duct influences the total losses. A cooling duct placed at the center of the conductor tends to increase the AC losses. In contrast, ducts positioned near the top or bottom of the conductor prove beneficial. For Case 15, adding a cooling duct near the top surface alone reduces total losses by approximately 20%. In contrast, Case 14, where the ducts are located at the center, results in a 2% increase in losses. Nevertheless, thermal and electromagnetic considerations must be carefully balanced in conductor design [17], [18].

B. Conductor Height Tuning at Specific Operating Point

Since conductor height significantly influences AC loss, four variants were investigated to explore this relationship. In Case 16, shown in Fig. 6, the height of each conductor was progressively reduced, resulting in lower total losses up to a certain point. Although DC resistance increases continuously with decreasing height, it becomes the dominant loss component beyond this minimum, causing the total losses to rise. Fig. 7 illustrates how loss varies with conductor height. Notably, the optimal height for minimizing loss differs between 1000 Hz and 2000 Hz. Using this approach, the total loss was reduced by 51.6% at 2000 Hz compared to the Case 12.

By reducing conductor height, the conductors can be brought closer together, which shortens the slot height and allows for 46.2% copper savings. This more compact winding layout may also enable a reduction in stator outer diameter or reallocation of space, potentially reducing iron usage or enhancing thermal performance, depending on design priorities and permissible flux densities. This configuration is shown in Case 17, where the slight increases in loss for layers 7 and 8 is due to the conductors being positioned closer to the slot

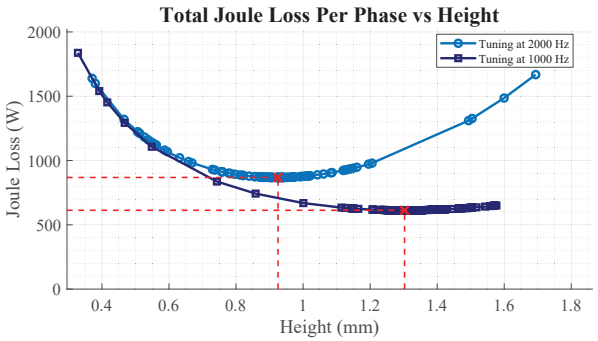

Fig. 7. Conductor height tuning at 2000 Hz (Case 16)

opening, thereby experiencing stronger radial flux.

Since loss tends to increase from the slot bottom toward the slot opening, each layer has a unique optimal conductor height that minimizes loss at a given frequency (2000 Hz in this study). In Case 18, it is assumed that each hairpin pair (layers 1-2, 3-4, etc.) shares the same optimized conductor height. This approach yields a total loss reduction of 56.3%.

Although manufacturing hairpins with different heights on each side is challenging, this constraint does not apply to additively manufactured conductors. In Case 19, all eight layers use individually optimized conductor heights. This results in a reduction of total loss by 57.2%. The transition between different heights can be implemented in the overhang region.

In Case 19, the optimization technique was performed sequentially, starting from layer 1 and progressing toward layer 8. Initially, the conductor heights of layers 2 to 8 were held constant while only the height of layer 1 was varied. The red dotted lines in Fig. 8 indicate the conductor height at which the joule loss reaches a minimum. In addition, green vertical lines are included to denote a $\pm 5\%$ range from this minimum value.

Once the optimal conductor height for layer 1 was determined (3.4 mm at 2000 Hz), it was fixed, and the conductor height for layer 2 was then varied to find its corresponding minimum loss. This iterative procedure was repeated layer by layer until layer 8 was reached.

It should be noted that the conductor tuning presented here is based solely on a single frequency (2000 Hz), and therefore does not reflect actual operating conditions. In practical applications, the entire drive cycle must be considered to accurately determine the optimal conductor height that minimizes total loss. However, such an analysis is beyond the scope of this paper. The primary objective of this section is to demonstrate how conductor height influences total losses, and how tuning can be employed in conjunction with the methods discussed in the subsequent sections.

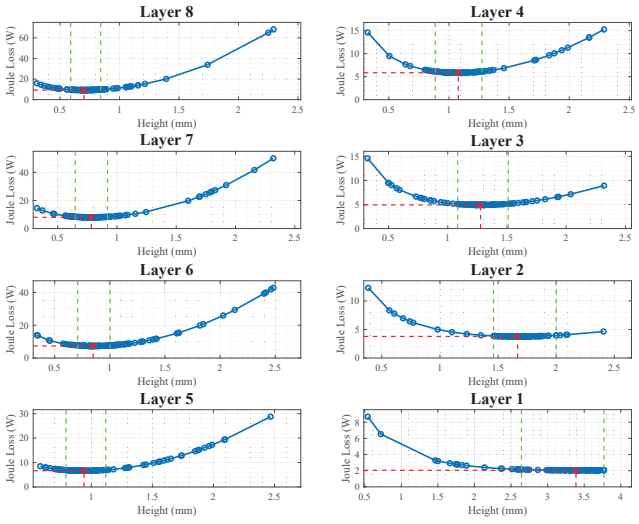

Fig. 8. Conductor height tuning at 2000 Hz (Case 19)

C. Segmented Conductor Design with Overhang Twisting

Another method to reduce AC losses involves segmenting the conductors and twisting the resulting subconductors (parallel strands) in the overhang region. This approach is commonly used in form-wound double-layer windings, where twisting naturally occurs as part of the winding process. Specifically, in double-layer windings, one side of the coil is placed in a lower slot layer while the return side is placed in the upper layer of a different slot [6]. As a result, the vertical positions of the conductors are inherently swapped between the two sides of the coil, effectively achieving a form of twisting that helps balance current distribution and reduce skin effect losses.

Fig. 9 presents the joule losses for each layer of the winding under four different conductor configurations (Cases 20-23). Each colored bar (in Fig. 9(a)) represents a different case, and the total height of the bar corresponds to the total loss in that layer. The vertical black lines segmenting each bar indicate the individual subconductor contributions to the total loss. These segments are arranged from left to right in the order of conductor position, starting from the slot bottom and progressing toward the slot opening.

In Case 20, the conductors are segmented into two without considering the overhang resistance. As shown in Fig. 9(a), this results in almost no change in total loss compared to the reference.

In Case 21, the same segmentation into two conductors is considered, but this time the DC resistance of the overhang is included in the calculation. This resistance plays a role in minimizing the skin effect, helping to reduce the AC losses. As a result, a loss reduction of 36.7% is observed. However, even great improvement is achieved when the conductors are twisted at the overhang.

Case 22 investigates this scenario: the two subconductors are twisted such that their vertical positions are swapped on the opposite side of the hairpin. This forces the current to redistribute more evenly between the segments, leading to a further reduction in loss by 63.1% compared to Case 12.

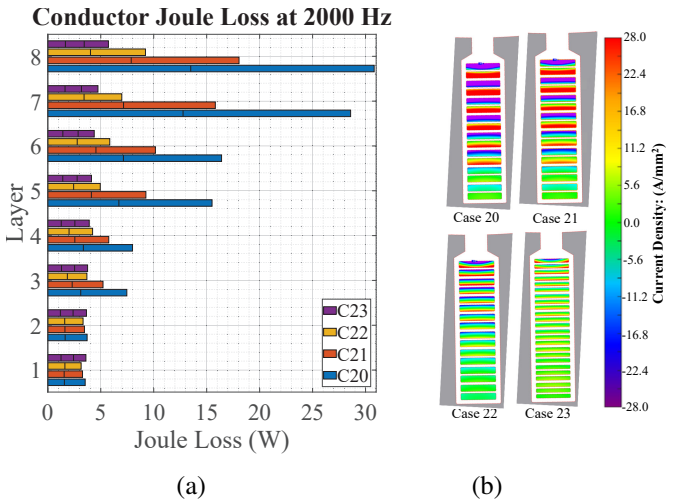

Fig. 9. Conductor segmentation: (a) loss density plot; (b) current density plot.

This demonstrates that while segmenting alone offers some benefit, twisting the conductors amplifies the effectiveness of the approach.

Further improvements can be achieved as shown in Case 23, where the conductor is split into three segments and twisted at the overhang. This configuration results in the largest reduction in loss, reaching 70%.

D. Combination of the Discussed Measures

As 80% of the total winding loss in the reference machine originates from layers 5 to 8, segmenting only these layers can yield similar benefits with reduced twisting effort. In Case 24 (Fig. 10), the conductor geometries in layers 1 to 4 are kept identical to the Case 12, while layers 5 and above are segmented and twisted. This approach results in a total loss reduction of 56.8% compared to the reference.

In Case 25, only layers 7 and 8 of Case 24 are further segmented into three subconductors, as these layers contribute most significantly to the overall loss. This targeted refinement leads to an additional loss reduction by 61.7%.

In Case 26, the configuration is based on Case 24, but with tuned conductor heights. Specifically, the bottom four layers (Layers 1-4) use the tuned conductor height obtained from Case 19, while the top four layers (Layers 5-8) are segmented and twisted in the overhang region, each using the optimal conductor height determined at 2000 Hz. Within each layer, all subconductors are assumed to have the same height. Although additive manufacturing allows for varying heights between subconductors, this study assumes uniform heights within a layer for simplicity.

The method for finding the optimum conductor height becomes more complex than in Case 19 when subconductors are involved. This is because the joule loss in each subconductor depends not only on the current passing through it, but also on the current flowing through subconductors located on the opposite side of the hairpin, i.e., in the layer above. For instance, the joule loss in layer 5 is influenced by both the ampere-turns below it (layers 1-4) and the current in layer 6 above.

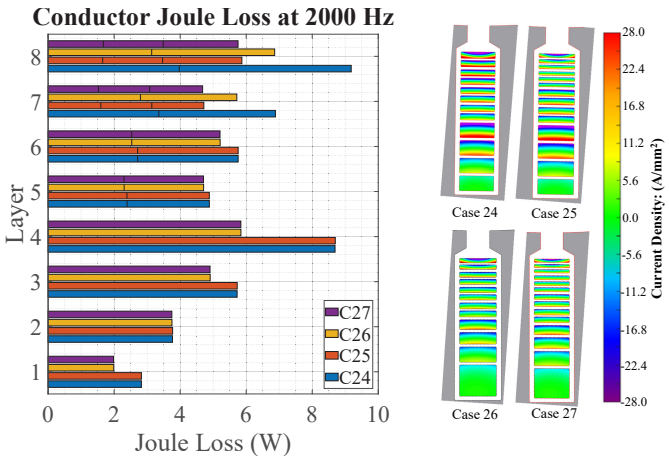

(a) (b)

Fig. 10. Combination of measures: (a) loss density plot; (b) current density plot.

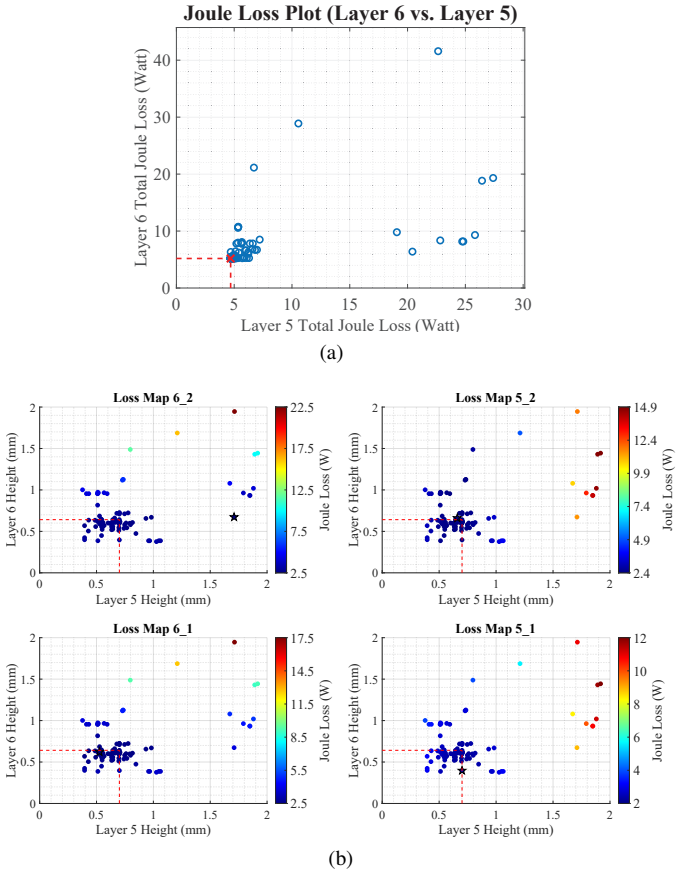

(a)

(b)

Fig. 11. Conductor height tuning at 2000 Hz (Case 26)

As a result, the conductor heights of the layer pairs 5–6 and 7–8 must be varied independently to obtain an optimal configuration. FEA is still used in this process, with the objective of minimizing the total loss in these two pairs. The optimization process begins with layers 5 and 6. Figure 11(a) presents a scatter plot of joule loss in layer 6 versus that in layer 5. The data points converge to a point indicated by red dotted lines, representing the optimal configuration. At this point, minimum losses of 4.69 W and 5.18 W are achieved for layers 5 and 6, respectively. Reducing the conductor heights further increases loss due to rising DC resistance.

This optimization process, illustrated in Fig.11, corresponds to a single optimization run. Different plots are generated for each subconductor (5_1, 5_2, 6_1 and 6_2), using the same scatter points for layers 5 and 6, but differing in joule loss due to positional variations within the slot.

It is important to highlight that the optimization goal was to minimize the total loss across all subconductors in layers 5 and 6, not to find the individual local minima. The global minimum occurs at conductor heights of 0.69 mm and 0.61 mm for layers 5 and 6, respectively, indicated by the red dotted lines in Fig. 11(b). However, individual subconductors exhibit local

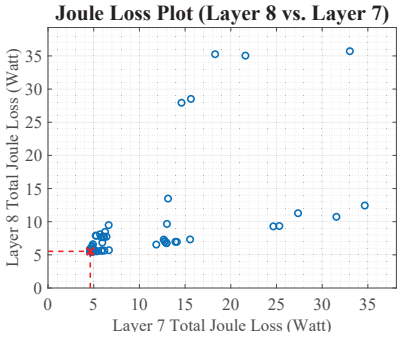

(a)

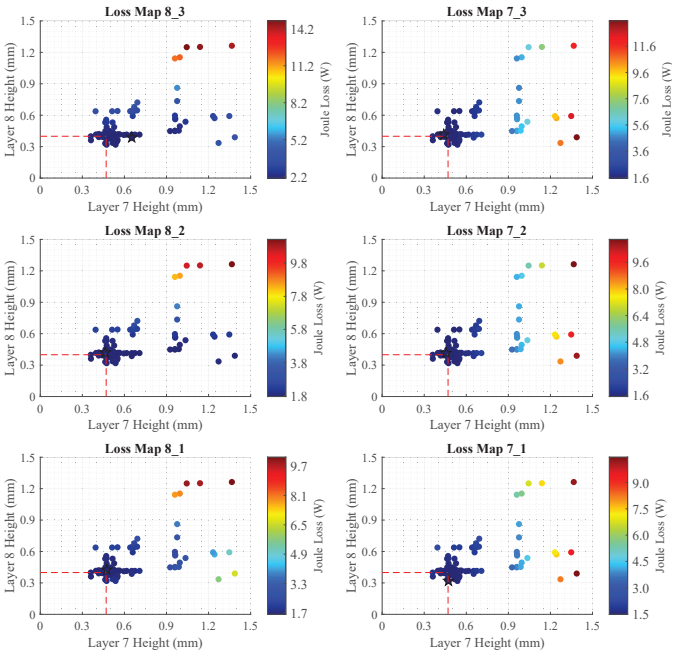

(b)

Fig. 12. Conductor height tuning at 2000 Hz (Case 27)

minima at slightly different heights, marked by star symbols in the plots.

A similar optimization approach was applied to layers 7 and 8, where the optimal conductor heights were found to be 0.48 mm and 0.4 mm, respectively. This configuration results in a total loss reduction of 19.1% compared to Case 24, and 65.1% compared to Case 12.

In Case 27, a similar approach is applied using Case 25 as the baseline. In this case, conductor heights across all layers are adjusted for 2000 Hz operation. The same optimization method is used, but with a new objective: to vary the conductor heights of layer 7 and 8 in order to minimize the total loss in those two layers.

Fig. 12 illustrates the results of this tuning. As a result, a loss reduction of 13.8% is achieved compared to Case 25, and a 67% reduction compared to Case 12.

Table IV summarizes the loss distributions (in watts) across the slot layers due to tangential flux for the discussed cases.

V. Conclusion

This study systematically investigated the key loss mechanisms in hairpin winding configurations and introduced targeted design interventions to mitigate them. Through the use of FEA simulations, it was shown that radial and tangential flux-induced AC losses disproportionately affect the top slot layers. Design variations, such as increasing fillet radius, incorporating semi-closed slot openings, and optimizing conductor geometry, achieved meaningful reductions in local and total losses. The greatest improvements were achieved by combining conductor segmentation with overhang twisting and frequency-specific height tuning. The final configuration demonstrated a 67% reduction in total joule loss compared to the reference. These results underline the importance of tailored conductor design, particularly when leveraging additive manufacturing, in achieving high efficiency in next-generation electric machines. Future work will address the integration of drive cycle-based optimization to extend these findings under real-world operating conditions.

TABLE IV
Summary of Joule Loss Distribution Across Slot Layers Under Tangential Flux Influence

	Conductor Fillet Radius Variations				Position of Cooling Ducts		Layer Specific Height Tuning			Four Layer Twisting		Four Layer Twisting with Height Tuning	
	Case 11		Case 12	Case 13	Case 14	Case 15	Case 17	Case 18	Case 19	Case 24	Case 25	Case 26	Case 27
	1000 Hz	2000 Hz	2000 Hz	2000 Hz	2000 Hz	2000 Hz	2000 Hz	2000 Hz	2000 Hz	2000 Hz	2000 Hz	2000 Hz	2000 Hz
L8	10.44	32.85	34.40	30.29	34.50	23.98	10.61	9.35	9.33	5.21 3.97	2.40 1.81 1.65	3.72 3.14	2.27 1.81 1.67
L7	7.99	23.27	24.61	21.23	24.82	19.25	8.52	8.10	8.07	3.53 3.35	1.58 1.54 1.60	2.92 2.80	1.60 1.55 1.52
L6	6.49	17.35	18.31	15.92	18.59	14.77	7.48	7.40	7.36	3.04 2.71	3.04 2.71	2.68 2.53	2.68 2.53
L5	5.27	12.54	13.15	11.65	13.48	10.97	6.67	6.69	6.65	2.49 2.39	2.49 2.39	2.41 2.30	2.41 2.30
L4	4.29	8.70	9.03	8.23	9.41	7.92	6.03	5.92	5.86	9.03	9.03	5.86	5.86
L3	3.56	5.81	5.94	5.67	6.35	5.62	5.55	5.00	4.93	5.94	5.94	4.93	4.93
L2	3.07	3.89	3.89	3.96	4.32	4.08	5.24	3.98	3.79	3.89	3.89	3.79	3.79
L1	2.83	2.93	2.86	3.11	3.30	3.29	5.07	2.56	2.07	2.86	2.86	2.07	2.07
Total Loss Per Slot (Watt)	43.93	107.35	112.18	100.06	114.78	89.88	55.19	49.01	48.06	48.41	42.93	39.15	36.99
Total Loss Per Phase (Watt)	702.88	1717.59	1794.94	1600.90	1836.41	1438.01	882.98	784.09	768.96	774.56	686.88	626.40	591.84

ACKNOWLEDGMENT

The authors would like to acknowledge the project partner, Dana Belgium N.V., for providing technical data, which enabled the study presented in this paper to reflect realistic design parameters.

REFERENCES

[1] B. Wex, B. Potzelberger, W. Gruber, and S. Silber, "Performance Comparison between Hairpin and Round Wire Winding for a 17,000 rpm PMSM," in *2022 International Conference on Electrical Machines (ICEM)*. Valencia, Spain: IEEE, Sep. 2022, pp. 1662–1668.

[2] T. Zou, D. Gerada, A. L. Rocca, M. Moslemin, A. Cairns, M. Cui, A. Bardalai, F. Zhang, and C. Gerada, "A Comprehensive Design Guideline of Hairpin Windings for High Power Density Electric Vehicle Traction Motors," *IEEE Transactions on Transportation Electrification*, vol. 8, no. 3, pp. 3578–3593, Sep. 2022.

[3] Y. Zhao, D. Li, T. Pei, and R. Qu, "Overview of the rectangular wire windings AC electrical machine," *CES Transactions on Electrical Machines and Systems*, vol. 3, no. 2, pp. 160–169, Jun. 2019.

[4] P. S. Ghahfarokhi, A. Podgornovs, A. J. Marques Cardoso, A. Kallaste, A. Belahcen, and T. Vaimann, "Hairpin Windings Manufacturing, Design, and AC Losses Analysis Approaches for Electric Vehicle Motors," in *2021 11th International Electric Drives Production Conference (EDPC)*. Erlangen, Germany: IEEE, Dec. 2021, pp. 1–7.

[5] L. Hausmann, F. Wirth, and J. Fleischer, "Opportunities of Model-Based Production-Oriented Design of Stators with Hairpin Winding," in *2020 10th International Electric Drives Production Conference (EDPC)*. Ludwigsburg, Germany: IEEE, Dec. 2020, pp. 1–8.

[6] G. Müller, K. Vogt, and B. Ponick, *Calculation of Electrical Machines (Berechnung elektrischer Maschinen) (in German)*. Weinheim: Wiley-VCH, 2007.

[7] G. Berardi, S. Nategh, N. Bianchi, and Y. Thioliere, "A Comparison Between Random and Hairpin Winding in E-mobility Applications," in *IECON 2020 The 46th Annual Conference of the IEEE Industrial Electronics Society*. Singapore, Singapore: IEEE, Oct. 2020, pp. 815–820.

[8] G. Berardi and N. Bianchi, "Design Guideline of an AC Hairpin Winding," in *2018 XIII International Conference on Electrical Machines (ICEM)*. Alexandroupoli: IEEE, Sep. 2018, pp. 2444–2450.

[9] A. M. Ajamloo, M. N. Ibrahim, and P. Sergeant, "A Review on Properties of 3D Printed Magnetic Cores for Electrical Machines: Additive Manufacturing Methods and Materials," in *2024 International Conference on Electrical Machines (ICEM)*. Torino, Italy: IEEE, Sep. 2024, pp. 01–07.

[10] C. Wachter, F. Haller, and F. Liebetrau, "Additive Manufactured Copper Conductors: Impedance Characteristics of Samples with Varying Density and Cross-section profile," in *2022 12th International Electric Drives Production Conference (EDPC)*. Regensburg, Germany: IEEE, Nov. 2022, pp. 1–5.

[11] R. Wrobel and B. Mecrow, "Additive Manufacturing in Construction of Electrical Machines – A Review," in *2019 IEEE Workshop on Electrical Machines Design, Control and Diagnosis (WEMDCD)*. Athens, Greece: IEEE, Apr. 2019, pp. 15–22.

[12] C. Noerenberg, J. Redlich, and B. Ponick, "Novel method for considering AC copper losses in traction motors," in *2020 International Conference on Electrical Machines (ICEM)*. Gothenburg, Sweden: IEEE, Aug. 2020, pp. 947–953.

[13] M. Soltani, S. Nuzzo, D. Barater, and M. D. Nardo, "Performance Analysis of a Permanent Magnet Motor with Continuous Hairpin Winding," in *2023 IEEE Workshop on Electrical Machines Design, Control and Diagnosis (WEMDCD)*. Newcastle upon Tyne, United Kingdom: IEEE, Apr. 2023, pp. 1–6.

[14] H.-C. Liu, H.-J. Lee, H.-S. Seol, S. Cho, J. Lee, and Y. J. Oh, "Optimal Slot Design of IPMSM in Railway With Independently Rotating Wheelsets," *IEEE Transactions on Magnetics*, vol. 55, no. 2, pp. 1–4, Feb. 2019.

[15] N. Bianchi and G. Berardi, "Analytical Approach to Design Hairpin Windings in High Performance Electric Vehicle Motors," in *2018 IEEE Energy Conversion Congress and Exposition (ECCE)*. Portland, OR, USA: IEEE, Sep. 2018, pp. 4398–4405.

[16] J. Pyrhönen, T. Jokinen, and V. Hrabovcová, *Design of Rotating Electrical Machines*, second edition ed. Chichester, West Sussex, United Kingdom: Wiley, 2014.

[17] C. Wohlers and B. Ponick, "First estimations of stator dimensions for permanent magnet synchronous machines with tooth-coil windings and direct liquid cooling," in *2020 International Conference on Electrical Machines (ICEM)*. Gothenburg, Sweden: IEEE, Aug. 2020, pp. 462–468.

[18] A. Selema, M. N. Ibrahim, and P. Sergeant, "Additively Manufactured Ultralight Shaped-Profile Windings for HF Electrical Machines and Weight-Sensitive Applications," *IEEE Transactions on Transportation Electrification*, vol. 8, no. 4, pp. 4313–4324, Dec. 2022.